Wall-Layer Onset and Whole-Depth Stability in Zero-Mean Heat-Flux Rayleigh–Bénard Convection

James Bjorken[1,*]

[1] SLAC National Accelerator Laboratory, Stanford University, Menlo Park, California 94025, USA
* Correspondence: bjbjorken@gmail.com

Abstract: The zero-mean modulation produces the zero-mean conductive temperature drop but allows wall-induced buoyancy amplification from the time-dependent wall gradient. The question posed in the investigation concerns the high-frequency asymptotic onset of the stability under prescribed harmonic heat flux modulation and specifically if the relation $\mathrm{Ra}_L \sim C_q\omega^2$ applies exclusively to the wall-layer criterion, whereas finite-amplitude stability holds throughout the depth of the layer. To find out the answer, the current study evaluates various characteristics such as neutral thresholds in terms of Floquet exponent, critical wavenumbers, high-frequency constants, nonlinear and strong stability thresholds, modified and alternative boundary conditions, variation in the Prandtl number, and DNS onset. The parameters are reformulated in terms of penetration depth, onset constant scaling, nonlinear separation constant, signed DNS threshold distance, and synchronization/subharmonic branches identification. The high-frequency onset is localized at first onset with $\mathrm{Ra}_L \sim C_q\omega^2$ and $k_c \sim \omega^{1/2}$ for no-slip and no-stress cases with $C_q = 22.58$ and $C_k = 12.44$. With $\omega = 100$, this yields respective onset estimates equal to 2.258×10^5 and 1.244×10^5. The above law alone does not guarantee nonlinear stability. The nonlinear thresholds depend on Pr and the distant boundary effects, whereas the DNS cases determine whether growth, decay, finite-amplitude onset, and branches apply.

Keywords: Rayleigh–Bénard convection; zero-mean heat flux; time-periodic forcing; penetration depth; nonlinear stability; Floquet analysis; thermal boundary conditions

Citation: James Bjorken. 2023. Wall-layer onset and whole-depth stability in zero-mean heat-flux Rayleigh–Bénard convection. *TK Techforum Journal (ThyssenKrupp Techforum)* 2023(2): 13–38.

Received: February-12-2023
Accepted: July-27-2023
Published: September-30-2023

Copyright: © 2023 by the authors. Licensee TK Techforum Journal (ThyssenKrupp Techforum). This article is an open access article distributed under the terms and conditions of the Creative Commons Attribution (CC BY) license (https://creativecommons.org/licenses/by/4.0/).

1. Introduction

The classic Rayleigh–Bénard model continues to serve as one of the key frameworks for understanding when buoyancy beats diffusion in a horizontal layer. Early theoretical studies established the threshold Rayleigh number, the possible form of perturbations, and the importance of mechanical conditions at the walls for a layer heated from below [1–3]. In subsequent work, the model became a benchmark scenario in finite-amplitude dynamics, heat-transport theory, turbulent thermal convection, and hydrodynamic stability [4,5]. What makes the system valuable today is the possibility to link threshold, boundary-layer behaviour, and transport with a relatively few non-dimensional quantities. Further studies of pattern formation and turbulent thermal convection confirm that the three observables should usually be considered in combination, rather than separately [6–8].

The threshold itself cannot provide a complete stability characterisation, as it marks only the onset of infinitesimal disturbances while the latter can only describe their growth. This is why linear onset is distinct from finite-amplitude decay which is concerned with the global stability of a solution subject to any perturbation of given type [9–11]. Boundary-layer properties and finite-amplitude cells are known to shift stability thresholds, and the corresponding physical information will be reflected through boundary conditions in what follows [12,13]. Meanwhile, energy and variational analysis demonstrates that the certificate of global stability can lie below the linear neutral curve, especially if the perturbation allows energy transfer unavailable to the unstable mode [14–17]. The present

study focuses on two closely related but conceptually different problems of linear stability and finite amplitude security.

There is a good reason to consider thermal boundary conditions. While the fixed-temperature and fixed-flux definitions are equivalent from a mathematical standpoint, this is not the case in real-life applications of convection, as well as in rigorous heat-transport bounds and experiments with thermal forcing [18,19]. The comparison of numerical and experimental results for turbulent convection shows that constant-temperature and constant-flux boundaries can generate similar heat transport under certain conditions but exhibit differences in other aspects [20,21]. More recent stability analyses of periodically and imperfectly heated systems underscore that both the admissible proof and dynamically generated flow may be sensitive to the nature of wall constraint [22–25].

Periodically changing forcing adds another level of complexity. When the boundary layer is no longer steady, the conductive profile is also periodic, the disturbance equations transform into the Floquet problem, and the dominant type of instability is determined by its temporal branch. The early work on time-varying thermal layers has established that modulated boundary conditions may shift onset threshold upward or downward depending on frequency and phase [26,27]. Later studies of unsteady convection, modulated layers, and modulated experiments confirmed the physicality of the temporal instability branch [28–30]. Stability analyses of periodically forced systems have also pointed out that the periodical neutral curve does not necessarily correspond to nonlinear global stability [31–33].

Zero-mean modulation stands out due to vanishing averaged temperature difference across the boundary layer. Although Or and Kelly showed that periodic heating can induce convection if the gradient changes sign over each cycle, the effect has been studied in other frequency ranges and boundary conditions as well [34–37]. Modern numerical studies of periodically cooled or periodically driven Rayleigh–Bénard convection also demonstrate that temporal forcing may alter the properties of plumes and boundary layer [38,39]. Experiments on radiatively forced convection highlight that non-conventional heating mechanism can lead to a new path of transition to strongly convective heat transport [40]. Such studies suggest the need for a stability analysis where the forcing is explicitly represented.

Stability analysis of a layer with harmonic heat flux reveals particularly interesting effects. A boundary layer driven by prescribed harmonic flux becomes increasingly thin when the frequency of modulating forcing grows. Christopher et al. performed this calculation based on Floquet–Fourier–Hill expansion, energy-moment stability criteria, family of boundary conditions, variations of Prandtl number, and DNS simulation [41]. The analysis relates to earlier bounds on time-varying thermal convection [42] and can utilise standard spectral methods for periodic problems [43,44]. As expected, the high-frequency threshold is proportional to ω^2 for the heat-flux problem but features a different exponent for zero-mean temperature forcing.

This study addresses the problem of how stability characteristics depend on the layer thickness for high-frequency forcing. To explore this question, we retain the following quantities as physically meaningful: Ra_L, k_c, Ra_A, Ra_S, branch identity, boundary condition, Pr, and DNS results. The findings demonstrate that the high-frequency limit of linear instability corresponds to the condition near the wall while nonlinear stability depends on the whole layer depth through Pr.

2. Local–global stability partition

The physical system considered is a Boussinesq fluid layer of thickness d, confined between two parallel plates. The bottom plate experiences an external harmonic heat flux with a vanishing time average, whereas the reference top wall remains at constant temperature. The acceleration due to gravity acts vertically downwards, resulting in the formation of a time-dependent conductive state with a destabilizing influence on its flow field in the neighbourhood of the heated boundary at high frequencies. The non-

dimensional quantities, namely frequency, Rayleigh number for the heat flux, and Prandtl number are

$$\omega = \frac{\omega^* d^2}{\kappa}, \qquad \mathrm{Ra} = \frac{\alpha g H d^4}{k\nu\kappa}, \qquad \mathrm{Pr} = \frac{\nu}{\kappa}. \tag{1}$$

It should now be evident from the definition of the Rayleigh number why there exists a d^4 term associated with it. Since our control parameter is heat flux rather than temperature difference, a direct comparison with fixed-temperature convection cannot be made by interchanging boundary conditions.

The non-dimensional forms of the perturbation Boussinesq equations in their representative form are

$$\nabla \cdot \boldsymbol{u} = 0, \qquad \mathrm{Pr}^{-1}(\partial_t \boldsymbol{u} + \boldsymbol{u} \cdot \nabla \boldsymbol{u}) = -\nabla p + \nabla^2 \boldsymbol{u} + \mathrm{Ra}\,\theta\, \boldsymbol{e}_z, \tag{2}$$

$$\partial_t \theta + \boldsymbol{u} \cdot \nabla \theta + w\, \partial_z T_B = \nabla^2 \theta. \tag{3}$$

The expression for $w\partial_z T_B$ provides a necessary connection between boundary forcing with zero mean value and buoyant production. The base-state temperature gradient even with its mean equal to zero can become in phase with an external disturbance during one period of forcing.

A two-dimensional disturbance may be expanded in a Floquet series,

$$\{w, \theta, p\}(x, z, t) = e^{ikx+\mu t} \sum_{n=-N}^{N} \{\widehat{w}_n(z), \widehat{\theta}_n(z), \widehat{p}_n(z)\} e^{int}, \tag{4}$$

with the linear threshold defined by

$$\mathrm{Ra}_L(\omega, \mathrm{Pr}, \mathcal{B}) = \min_k \left\{ \mathrm{Ra} : \max_{n,k} \Re[\mu_n(k, \mathrm{Ra}, \omega, \mathrm{Pr}, \mathcal{B})] = 0 \right\}. \tag{5}$$

It is the minimisation over k that requires both critical values to be considered simultaneously. Boundary condition identification by $\mathcal{B}$ is kept because the effect of the modulated wall and the other wall is not identical within local and global formulations.

The branch-resolved neutral solution may be expressed as

$$\mathrm{Ra}_L(\omega) = \min\{\mathrm{Ra}_L^{(s)}(\omega), \mathrm{Ra}_L^{(sh)}(\omega)\}, \qquad \sigma_b(\omega) = \begin{cases} \mathrm{s}, & \mathrm{Ra}_L^{(s)} < \mathrm{Ra}_L^{(sh)}, \\ \mathrm{sh}, & \mathrm{Ra}_L^{(sh)} < \mathrm{Ra}_L^{(s)}, \\ \mathrm{co}, & \mathrm{Ra}_L^{(s)} = \mathrm{Ra}_L^{(sh)}. \end{cases} \tag{6}$$

In this way, the notation σ_b does not serve any merely aesthetic purpose; it stands for an actual value obtained from a comparison of two Floquet spectra and signifies that in the vicinity of equality, the behavior of time could vary greatly without a large shift in the neutral boundary.

The stability region for the analysis used is

$$\mathcal{D} = \{\mathrm{Ra}_L,\ k_c,\ \mathrm{Ra}_A,\ \mathrm{Ra}_S,\ \mathcal{B},\ \mathrm{Pr},\ \mathrm{Ra}_o,\ \sigma_b,\ \mathcal{R}_{DNS}\}, \tag{7}$$

Where σ_b refers to the time branch label and $\mathcal{R}_{DNS}$ refers to the numerical response that is observed. This notation in terms of sets does not imply any kind of independence in terms of measurements. This notation simply refers to what kinds of stability criteria are distinguished: neutrality criteria, constants, branches, nonlinear limit, and DNS cases have their own physical meanings.

Finite amplitude formulation may be described using an energy functional

$$\mathcal{E}_\beta(t) = \frac{1}{2\mathrm{Pr}} \|\boldsymbol{u}(t)\|_2^2 + \frac{\beta}{2} \|\theta(t)\|_2^2, \tag{8}$$

for which a nonlinear stability calculation seeks constants $\beta > 0$ and $c_\beta > 0$ such that

$$\frac{d\mathcal{E}_\beta}{dt} \leq -c_\beta \left(\|\nabla \boldsymbol{u}\|_2^2 + \|\nabla \theta\|_2^2 \right) + \mathrm{Ra}\, \mathcal{P}_\beta(t), \qquad \langle \mathcal{P}_\beta \rangle_T \leq 0. \tag{9}$$

The above equation captures the mathematics behind the duplication of Ra_A and Ra_S to Ra_L. The neutral case corresponds to the largest Floquet multiplier while the nonlinear threshold depends on the controllability of the production operator $\mathcal{P}_\beta$.

Table 1 distinguishes between the terms belonging to infinitesimal onset and the terms belonging to finite-amplitude decay. Linear terms identify the first perturbation that is capable of growing, while nonlinear terms indicate whether finite perturbations can be excluded. Separation of these terms ensures that the instability at high frequencies is not confused with a stability proof.

Table 1. Stability quantities.

Quantity group	Principal quantities	Physical role	Question resolved
Neutral onset	$\mathrm{Ra}_L(\omega)$ and $k_c(\omega)$ for synchronous and subharmonic branches	Locates the first infinitesimal disturbance and its horizontal scale	Where does the wall-layer trigger begin?
Wall-layer scaling	$\mathrm{Ra}_L\omega^{-2}$ and $k_c\omega^{-1/2}$ for heat-flux forcing	Tests the penetration-depth onset condition	Which boundary sets the high-frequency constant?
Nonlinear separation	$\mathrm{Ra}_A(\omega, \mathrm{Pr})$ and $\mathrm{Ra}_S(\omega, \mathrm{Pr})$	Measures finite-amplitude exposure below Ra_L	How far is guaranteed decay from onset?
DNS threshold placement	Growth rates, trajectories, and branch-sensitive runs	Compares threshold signs with time-dependent response	Does the time-dependent solution preserve the hierarchy?

The physical interpretation of the two length scales considered below is set by the configuration sketch. The total layer thickness defines the non-dimensionalisation and the overall energy balance, whereas the oscillatory thermal boundary layer corresponds to the high-frequency contribution. This distinction explains why the subsequent stability analysis fails to provide a common stability parameter for all possible perturbations. Heat-flux modulation geometry is presented in Figure 1.

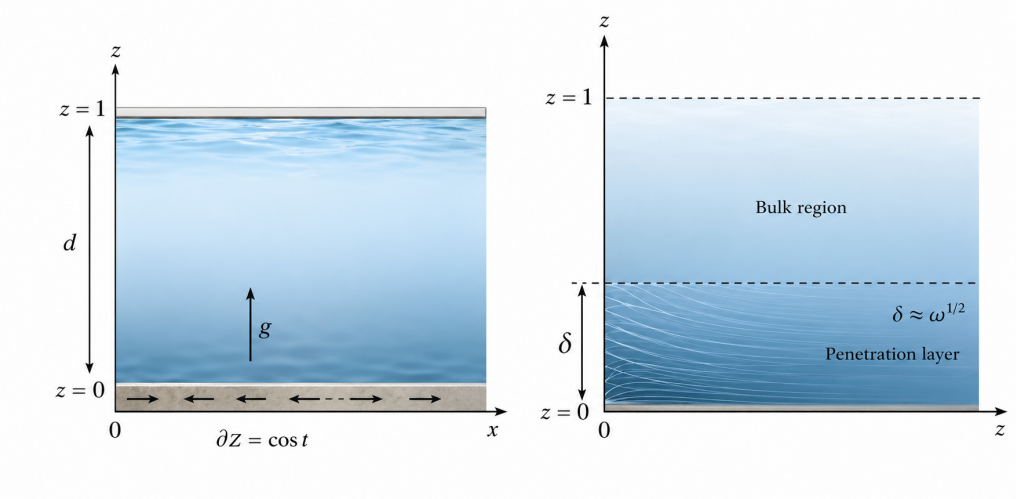

Figure 1. Heat-flux modulation geometry.

The camera-view sketches in Figures 2-4 provide physical insight into the definition of the non-dimensional geometry. The cell sketch provides information on the location of fixed temperature and heat flux walls, whereas the wall-layer sketch justifies the choice of oscillatory heating as a thin layer. Finally, the planform sketch relates the critical wavelength to the actual horizontal size of cellular convection. This placement of sketches is due to the fact that the considered stability parameters gain their meaning after separation of the total thickness and the wall layer. In Figure 5, the diagnostic procedure route separates the two cases based on stability classes. For the top branch, δ, Λ_q, Ra_L, and k_c are employed for the determination of the onset criterion for the near-wall instability. In the bottom branch, the

separation of Ra_A and Ra_S from Ra_L is considered, where the nonlinear stability can alter the classification of a situation even if the trigger for the linear instability is not met yet.

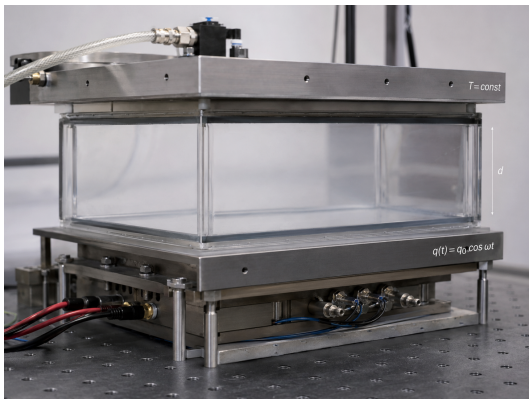

Figure 2. Cell geometry.

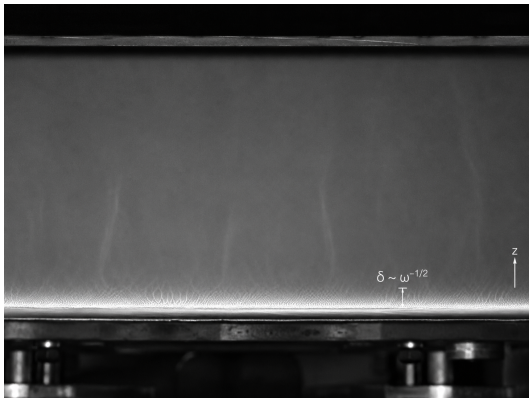

Figure 3. Wall-layer image.

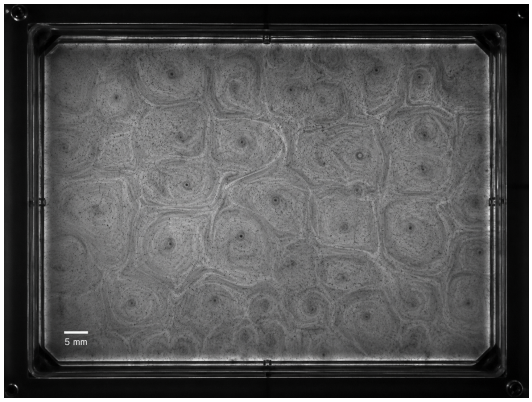

Figure 4. Planform cells.

For the high-frequency limit, the conductive base profile gradient takes the leading order form

$$\partial_z T_B(z,t) \approx e^{-z\sqrt{\omega/2}} \cos\left(t - z\sqrt{\frac{\omega}{2}}\right). \tag{10}$$

This expression accounts for both localization and the phase shift. The exponentially varying term limits the maximum destabilizing gradient at the forced wall, whereas the oscillatory behavior is indicative of the fact that depths in the water column do not have the same phase.

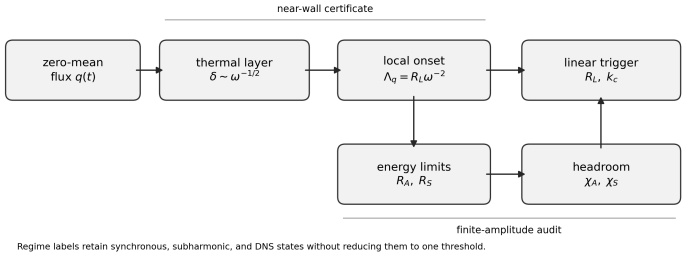

Figure 5. Calculation path.

The active layer thickness and matched horizontal scale are thus

$$\delta \sim \omega^{-1/2}, \qquad \eta = \frac{z}{\delta}, \qquad k\delta = O(1). \tag{11}$$

The last relation of (11) indicates that the most dangerous perturbation shrinks along the horizontal direction as the thickness of the thermal boundary layer decreases. This relation also provides the physical cause for the observed dependence $k_c \sim \omega^{1/2}$.

For heat-flux modulations, the wall-layer Rayleigh number locally is

$$\mathrm{Ra}_\delta^{(q)} \propto \mathrm{Ra}\delta^4 \propto \mathrm{Ra}\omega^{-2}, \qquad \mathrm{Ra}_L^{(q)}(\omega) \approx C_q(\mathcal{B}_m)\,\omega^2. \tag{12}$$

This forms the heart of the near-wall certificate. Namely, the condition for the high-frequency cut-off is based on using the Rayleigh number for the heat flux within the penetration region rather than assuming that the entire layer constitutes a classically forced Rayleigh–Bénard layer.

A finite-amplitude measure of the forcing level can be written as

$$\chi_A = \frac{\mathrm{Ra}_L - \mathrm{Ra}_A}{\mathrm{Ra}_L}, \qquad \chi_S = \frac{\mathrm{Ra}_L - \mathrm{Ra}_S}{\mathrm{Ra}_L}, \qquad \Lambda_q = \mathrm{Ra}_L\omega^{-2}. \tag{13}$$

In this definition, Λ_q is a local criterion, while χ_A and χ_S are measures of global separation. If either of these values is positive, a nonlinear decay threshold will exist below the neutral line such that linear subcriticality is insufficient.

If a DNS Rayleigh number Ra_o is known, the following ratios apply:

$$\mathcal{S}_L = \frac{\mathrm{Ra}_o}{\mathrm{Ra}_L}, \qquad \mathcal{S}_A = \frac{\mathrm{Ra}_o}{\mathrm{Ra}_A}, \qquad \mathcal{S}_S = \frac{\mathrm{Ra}_o}{\mathrm{Ra}_S}. \tag{14}$$

These ratios are intentionally asymmetric in interpretation. The condition $\mathcal{S}_L < 1$ only says that infinitesimal growth is not predicted, whereas $\mathcal{S}_A > 1$ or $\mathcal{S}_S > 1$ identifies exposure relative to a nonlinear threshold.

A case lying between strong nonlinear stability and linear onset can be placed on the coordinate

$$\mathcal{M}(\mathrm{Ra}_o) = \frac{\mathrm{Ra}_o - \mathrm{Ra}_S}{\mathrm{Ra}_L - \mathrm{Ra}_S}, \qquad 0 < \mathcal{M} < 1. \tag{15}$$

This coordinate records whether a case is closer to the guaranteed-decay side of the interval or to the infinitesimal-onset side. That distinction becomes useful when the DNS trajectories are interpreted below.

3. Results and Discussion

3.1. Thresholds without scaling and selection of the branches

The unscaled threshold map needs to be interpreted before the high-frequency asymptote is introduced. The curve retains the information about the competition in frequencies between synchronous and subharmonic branches, as well as about the location of nonlinear

limits relative to the onset of the instability. Omitting such data prematurely obscures the temporal evolution difference between steady thresholds and zero-mean modulation.

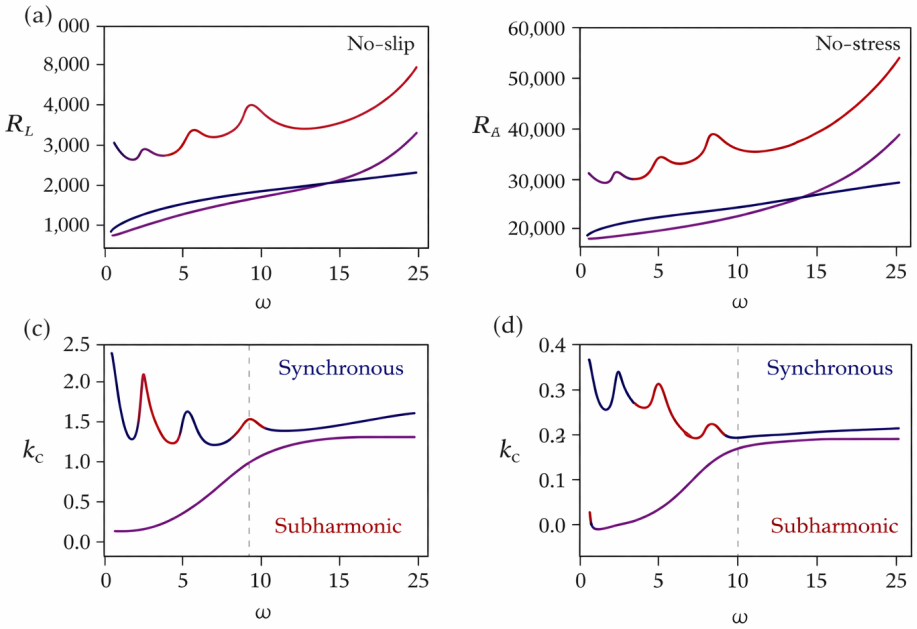

Figure 6. Raw thresholds.

The raw unscaled threshold map in Figure 6 illustrates that the heat-flux instability exhibits at least two hierarchies of organisation. High-frequency trend converges towards the asymptotic law fast enough, yet the low-frequency part is still structured enough for branch distinction. The panels corresponding to the critical wavenumbers are also essential since they illustrate that the most unstable horizontal length scales decrease with frequency. Such a frequency-dependent contraction is one of the key features of the neutral-curve behaviour explained by the penetration-depth mechanism.

The separation between the wall-layer trigger Ra_L and the nonlinear thresholds can be identified as the first separation signal. Should stability depend only on the wall-layer triggers, then the nonlinear curves will not differ from each other and will remain simple offsets of the neutral curve. The difference in position means that finite-amplitude robustness depends on the energy distribution of the entire boundary layer.

The branch margin needed for mathematical interpretation of the same result is

$$\mathcal{J}(\omega) = \frac{\mathrm{Ra}_L^{(sh)}(\omega) - \mathrm{Ra}_L^{(s)}(\omega)}{\min\{\mathrm{Ra}_L^{(s)}(\omega), \mathrm{Ra}_L^{(sh)}(\omega)\}}. \tag{16}$$

A positive value of $\mathcal{J}$ identifies synchronous onset, a negative value identifies subharmonic onset, and $|\mathcal{J}| \ll 1$ identifies a branch-sensitive band. This equation converts the visual crossing of neutral branches into a signed stability result.

The nonlinear offset can be written in absolute and relative form as

$$\Delta_A^{NL} = \mathrm{Ra}_L - \mathrm{Ra}_A, \qquad \Delta_S^{NL} = \mathrm{Ra}_L - \mathrm{Ra}_S, \qquad \frac{\Delta_A^{NL}}{\Delta_S^{NL}} = \frac{\chi_A}{\chi_S} \quad (\chi_S \neq 0). \tag{17}$$

These first two quantities capture the distance between onset and a nonlinear decay in terms of Rayleigh numbers, whereas the final fraction determines if asymptotics and strong nonlinearities open up the same range of exposure.

The split up neutral plots of Figures 7 through 8 are much more clear than one plot overloaded with information. The chosen neutral curve in Figure 7 is where the onset of the instability is determined, and the growth of the critical horizontal wavenumber is shown in

Figure 8. In addition to this, heat flux plots of Figures 9 and 10 show the same information in log space.

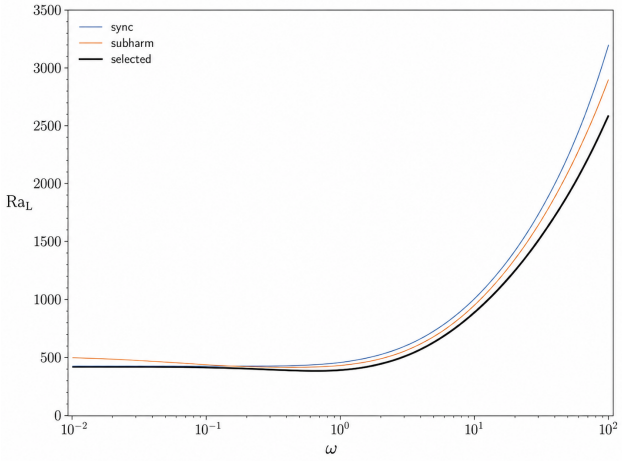

Figure 7. Neutral envelope.

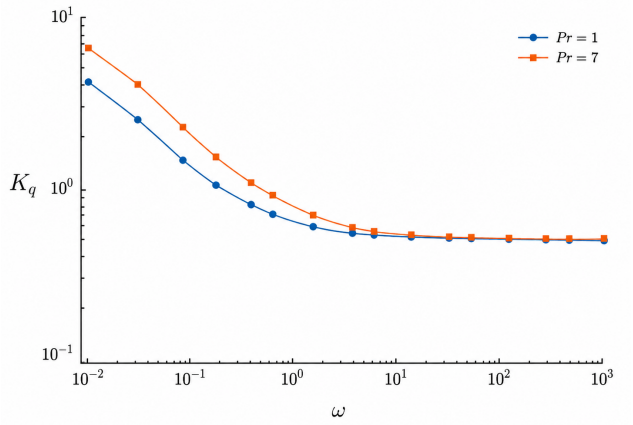

Figure 8. Wavenumber branch.

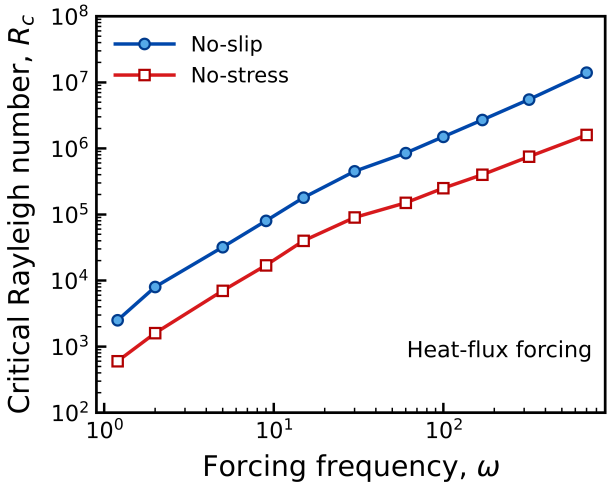

Figure 9. Heat-flux thresholds.

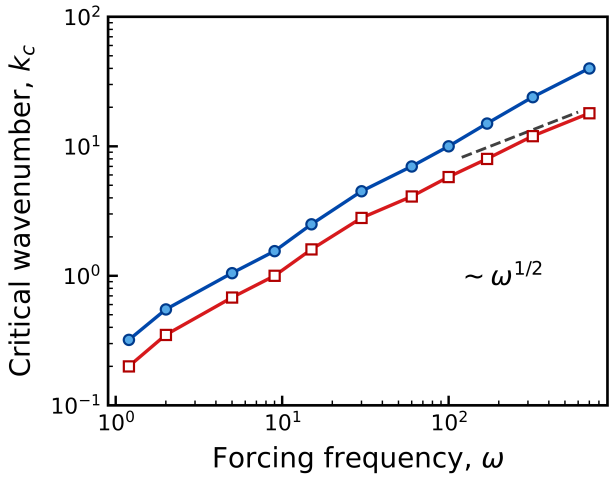

Figure 10. Wavenumber growth.

3.2. Collapse of wall-layer and contrast of forcing type

The high-frequency region of the analysis is confirmed by comparing $\mathrm{Ra}_L\omega^{-2}$ and $k_c\omega^{-1/2}$. With the penetration depth argument as the correct local explanation, these scaled parameters should converge to constant values mostly controlled by the modulated-wall criterion. Such a test is more stringent than noting the increase of the unscaled critical threshold with frequency.

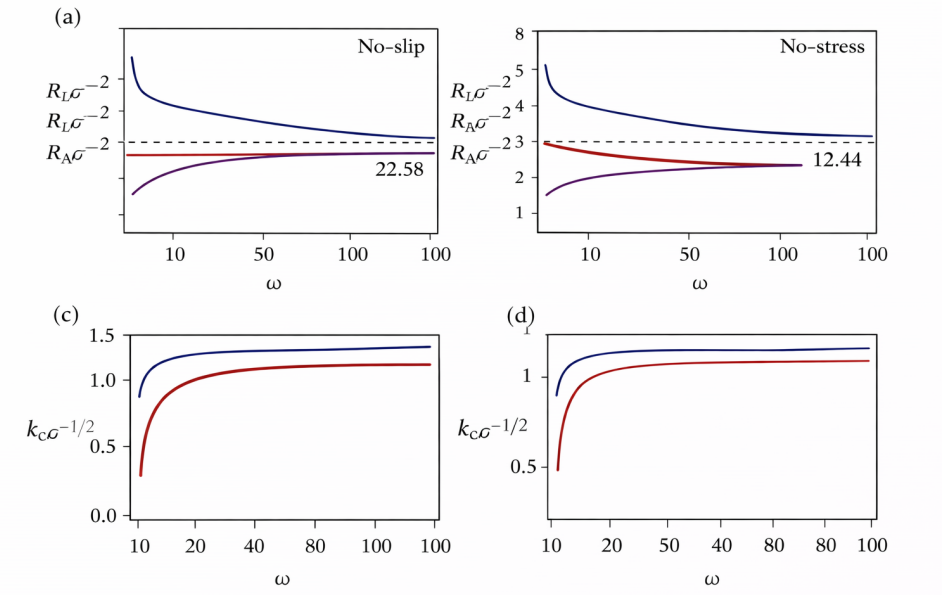

Figure 11. Wall-layer collapse.

In Figure 11, we find the wall-layer collapse consistent with the local answer to the research question. At high enough frequencies, the scaled threshold converges to two different constants depending on the nature of the modulated boundary conditions. The wavenumber scaling is also consistent with finite perturbations that are always confined within the shrinking active layer. Such consistency allows us to use Λ_q as a criterion for infinitesimal onset.

Figure 11 also provides insight into the limitations of the scaled certificate. The scaled linear relation will reveal the boundary condition leading to infinitesimal onset, but not whether the decay takes place with a finite disturbance. To learn this latter information, we need to compare the energy thresholds and their impact on DNS.

The convergence can be expressed asymptotically,

$$\Lambda_q(\omega) = \mathrm{Ra}_L\omega^{-2} = C_q + C_{q,1}\omega^{-1/2} + O(\omega^{-1}), \qquad K_q(\omega) = k_c\omega^{-1/2} = K_{q,0} + O(\omega^{-1/2}). \tag{18}$$

The first relation produces the limiting constants in Table 2; the second relation states that the dimensional wavelength contracts with the same square-root law as the thermal penetration layer. Thus the high-frequency limit supplies two results, not one: a Rayleigh-number law and a horizontal-scale law.

For the two heat-flux mechanical conditions, the limiting constants give

$$C_{q,NS} = 22.58, \qquad C_{q,NF} = 12.44, \qquad \frac{C_{q,NS}}{C_{q,NF}} = 1.815, \qquad \frac{C_{q,NS} - C_{q,NF}}{C_{q,NS}} = 0.449. \tag{19}$$

The rigid-wall constant is therefore about 81.5% larger than the stress-free constant, while the stress-free reduction measured against the rigid-wall value is about 44.9%.

Table 2 distinguishes between two processes sharing a similar diffusion layer thickness but with a different scaling of the Rayleigh number. The forcing through heat flux corresponds to ω^2 scaling, while forcing by temperature at the boundaries corresponds to $\omega^{3/2}$. Thus, it is not possible to convert the prescribed-temperature stability criterion to the prescribed-flux form via adjustment of just the numerical constant.

Table 2. High-frequency constants.

Forcing class	Modulated-wall condition	Linear asymptote	Constant	Interpretation
Heat flux	No-slip	$\mathrm{Ra}_L\omega^{-2} \to C_q$	22.58	rigid wall raises local onset
Heat flux	No-stress	$\mathrm{Ra}_L\omega^{-2} \to C_q$	12.44	stress-free wall lowers local onset
Boundary temperature	No-slip	$\mathrm{Ra}_L\omega^{-3/2} \to C_T$	27.86	prescribed-temperature comparison
Boundary temperature	No-stress	$\mathrm{Ra}_L\omega^{-3/2} \to C_T$	18.38	stress-free temperature comparison

The normalized subplots in Figures 12–13 display the two sides of the high-frequency statement: $\mathrm{Ra}_L\omega^{-2}$ tends to a constant dependent on the boundary, whereas $k_c\omega^{-1/2}$ converges to another constant for the horizontal scale. The results of this kind are presented in Figures 14 and 15, separately as individual plots for the no-slip and no-stress heat-flux conditions. The forcing comparison shown in Figure 16 ensures that heat flux and prescribed temperature forcing are considered independently because they have distinct critical exponents.

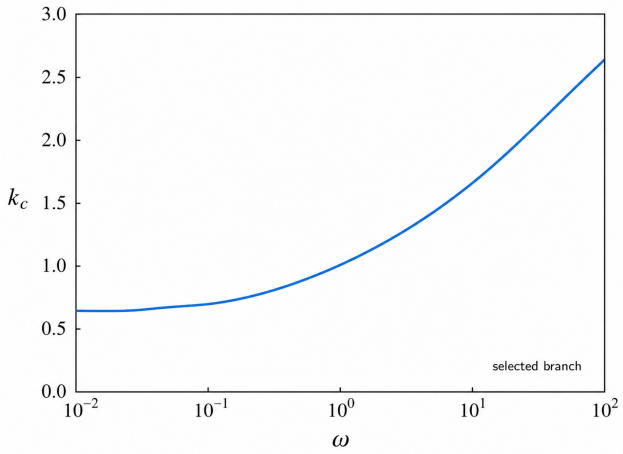

Figure 12. Flux-scale limit.

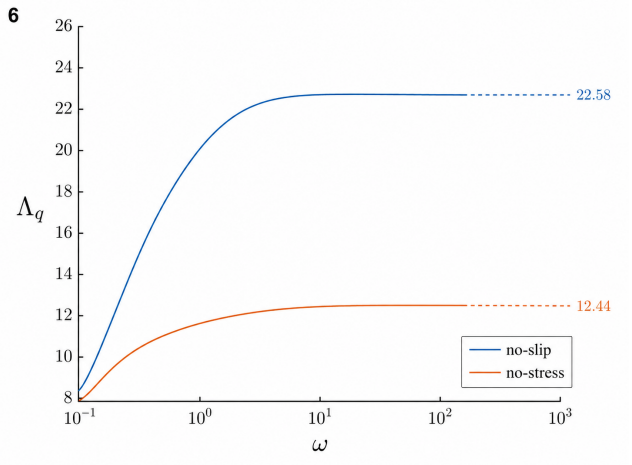

Figure 13. Wavenumber limit.

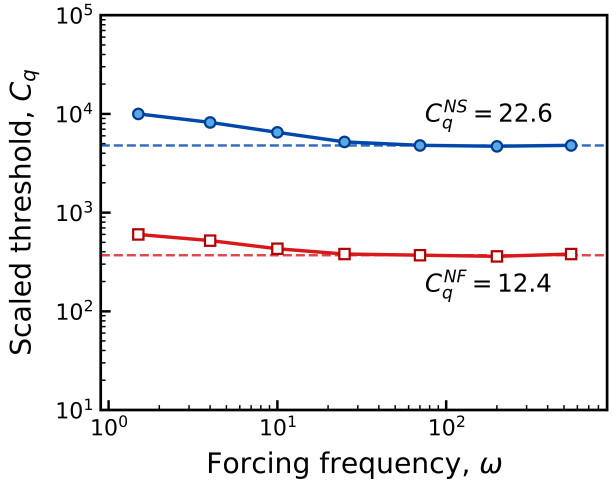

Figure 14. Scaled Rayleigh constants.

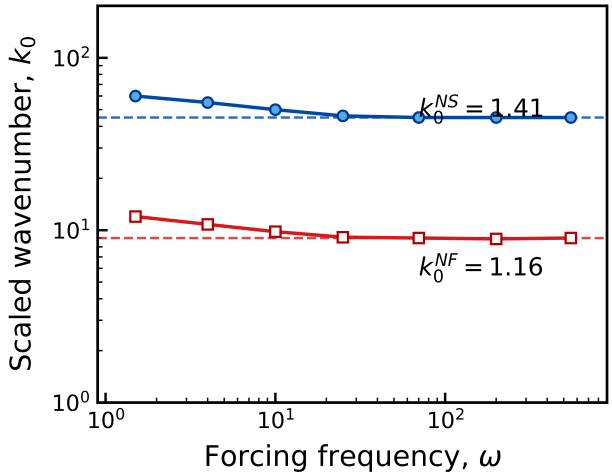

Figure 15. Scaled wavenumber constants.

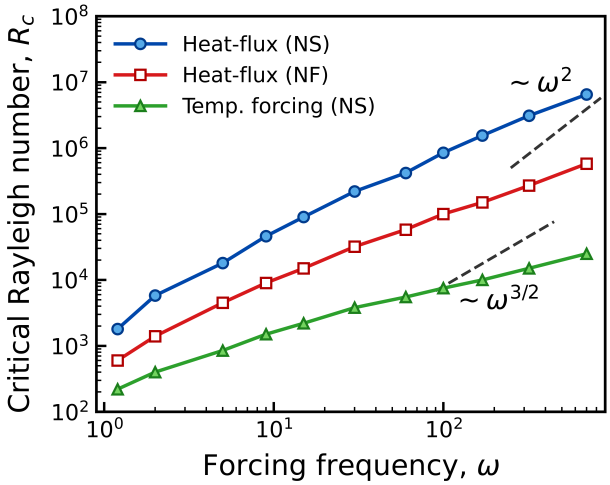

Figure 16. Forcing contrast.

3.3. Numerical values at $\omega = 100$

A margin calculation is more useful when the asymptotic constants are converted into numbers. For $\omega = 100$, the heat-flux thresholds are

$$\begin{aligned} \mathrm{Ra}_{L,\mathrm{NS}}^{(q)}(100) &\approx 22.58(100)^2 = 2.258 \times 10^5, \\ \mathrm{Ra}_{L,\mathrm{NF}}^{(q)}(100) &\approx 12.44(100)^2 = 1.244 \times 10^5. \end{aligned} \tag{20}$$

The no-slip wall therefore increases the local onset estimate by about 8.14×10^4 Rayleigh-number units at this frequency. The ratio $22.58/12.44 \approx 1.82$ gives an 82% wall-condition effect after the dominant frequency dependence has already been removed.

The associated penetration-depth estimates are

$$\delta(100) = 0.100, \qquad \ell_e(100) = \sqrt{\frac{2}{100}} = 0.141, \qquad z_{1\%}(100) = \ln(100)\sqrt{\frac{2}{100}} = 0.651. \tag{21}$$

The first one is the thickness of similarity, the second is the distance e-folding of the leading exponential term, and the third is the depth where the leading gradient of the flow is one percent of that near the wall. This calculation shows why onset of high frequencies is wall biased but a thermal tail is still important in estimating full-depth energy.

Contrast in forcing type at the same frequency is

$$\frac{\mathrm{Ra}_{L,\mathrm{NS}}^{(q)}}{\mathrm{Ra}_{L,\mathrm{NS}}^{(T)}} \approx \frac{22.58\omega^2}{27.86\omega^{3/2}} = 0.811\omega^{1/2}, \qquad \frac{\mathrm{Ra}_{L,\mathrm{NF}}^{(q)}}{\mathrm{Ra}_{L,\mathrm{NF}}^{(T)}} \approx 0.677\omega^{1/2}. \tag{22}$$

At $\omega = 100$, the ratios are approximately 8.10 and 6.77. The comparison demonstrates that rapid heat-flux forcing is substantially harder to destabilise than the corresponding boundary-temperature problem because the local buoyancy measure differs, not because the diffusion length differs.

The logarithmic sensitivity of the heat-flux threshold is

$$\frac{\partial \ln \mathrm{Ra}_L^{(q)}}{\partial \ln \omega} = 2, \qquad \frac{\partial \mathrm{Ra}_L^{(q)}}{\partial \omega} = 2C_q\omega, \qquad \frac{\Delta \mathrm{Ra}_L^{(q)}}{\mathrm{Ra}_L^{(q)}} \approx \frac{\Delta C_q}{C_q} + 2\frac{\Delta\omega}{\omega}. \tag{23}$$

A five percent change in forcing frequency produces an approximately ten percent change in the local onset estimate before uncertainty in C_q is considered. For the no-slip case at

$\omega = 100$, the slope is 4516 Rayleigh-number units per unit increase in ω; for the no-stress case it is 2488.

The horizontal-scale result follows from the same square-root law:

$$\frac{k_c(100)}{k_c(25)} \approx \left(\frac{100}{25}\right)^{1/2} = 2, \qquad \frac{\lambda_c(100)}{\lambda_c(25)} = \frac{k_c(25)}{k_c(100)} \approx 0.5. \tag{24}$$

Increasing the forcing frequency from 25 to 100 therefore doubles the critical wavenumber and halves the horizontal wavelength of the first high-frequency disturbance, even before any finite-amplitude criterion is applied.

The numbers listed in Table 3 make the scaling expression a quantitative stability analysis. A specified Rayleigh number can be evaluated against the local triggering criteria, the forcing-like contrast, and the frequency dependence before any consideration of the nonlinear limits or temporal simulations.

Table 3. Values at $\omega = 100$.

Calculated quantity	Numerical value	Physical interpretation
Similarity thickness $\delta = \omega^{-1/2}$	0.100	active layer is one tenth of the full depth
E-folding depth $\ell_e = \sqrt{2/\omega}$	0.141	leading base-gradient amplitude falls by e^{-1}
No-slip heat-flux threshold $22.58\omega^2$	2.258×10^5	local onset estimate for a rigid modulated wall
No-stress heat-flux threshold $12.44\omega^2$	1.244×10^5	local onset estimate for a stress-free modulated wall
No-slip/no-stress heat-flux ratio	1.82	mechanical constraint raises the asymptotic constant
No-slip heat-flux/temperature ratio	8.10	flux forcing is harder to destabilise at this frequency
No-slip frequency slope $2C_q\omega$	4516	local threshold gain per unit frequency

The magnitude information shown in Figure 17 converts the $\omega = 100$ calculations into a quantitative form. The comparison preserves the scaling numbers, wall layer thickness, exponential distance, one percent depth, faraway wall strength, and tail integral at the same order of magnitude, making it possible for the reader to appreciate the difference between the local trigger and the global energy.

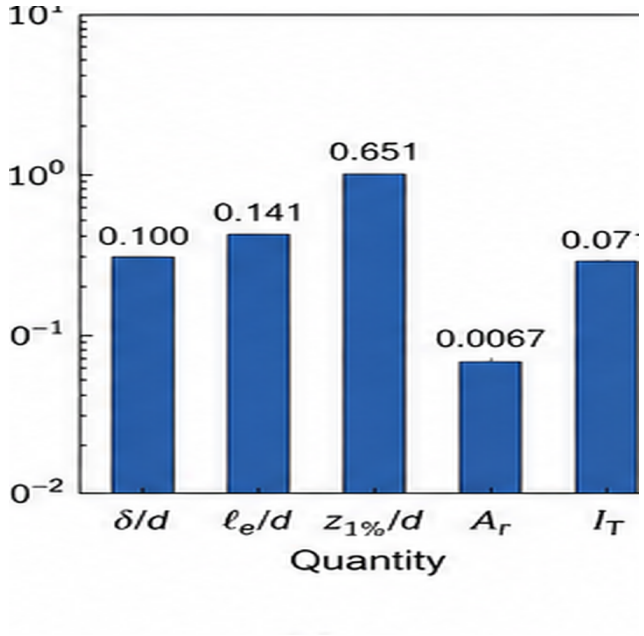

Figure 17. Values at $\omega = 100$.

3.4. Prandtl-number nonlinear separation

A sweep with respect to the Prandtl number checks the hypothesis that the local condition also determines the onset of nonlinear excitation. The dependence of $\mathrm{Re}_{\mathrm{Lin}}(\mathrm{Pr})$

and $\mathrm{Re}_{\mathrm{lim}}$ on the Prandtl number is dissimilar at $\omega_c = 100$. Hence, the nonlinear separation does not depend solely on the penetration depth.

The increasing gap in Figure 18 means that the low Prandtl number problem cannot be simplified as a high-frequency wall-law behavior. Heat and momentum transfer at two very different characteristic timescales means that the energy method cutoff captures the whole spectrum. Consequently, a situation might occur where the condition is less than Ra_L but still near a nonlinear boundary.

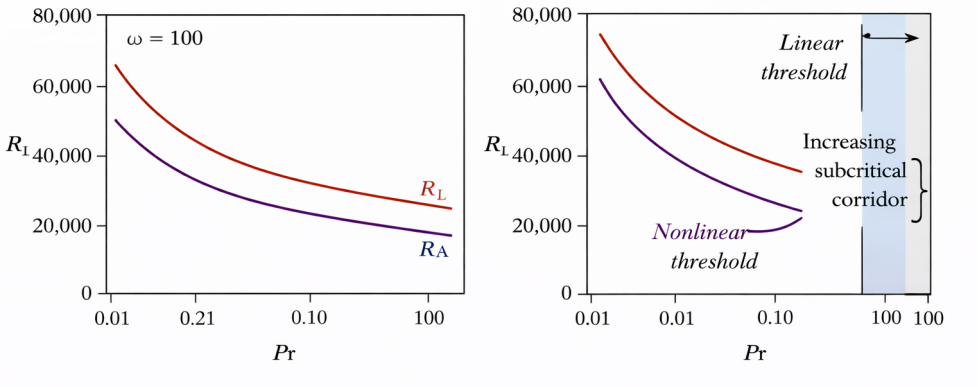

Figure 18. Prandtl separation.

The difference can be expressed by thermal and viscous oscillatory lengths,

$$\delta_T = \omega^{-1/2}, \qquad \delta_\nu = \left(\frac{\mathrm{Pr}}{\omega}\right)^{1/2}, \qquad \frac{\delta_\nu}{\delta_T} = \mathrm{Pr}^{1/2}. \tag{25}$$

At $\omega = 100$, this gives

$$\delta_\nu(\mathrm{Pr} = 0.1) = 0.0316, \qquad \delta_\nu(\mathrm{Pr} = 1) = 0.100, \qquad \delta_\nu(\mathrm{Pr} = 10) = 0.316. \tag{26}$$

These values show why the nonlinear threshold is Prandtl-sensitive even when the thermal penetration thickness is fixed by frequency. The kinetic-energy drainage length changes by an order of magnitude across the displayed Prandtl range.

The corresponding separation elasticity is

$$\mathcal{E}_{A,\mathrm{Pr}} = \frac{\partial \ln(\mathrm{Ra}_L/\mathrm{Ra}_A)}{\partial \ln \mathrm{Pr}}, \qquad \mathcal{E}_{S,\mathrm{Pr}} = \frac{\partial \ln(\mathrm{Ra}_L/\mathrm{Ra}_S)}{\partial \ln \mathrm{Pr}}. \tag{27}$$

Any nonvanishing quantity of the two nonlinear margins will serve as a mathematical proof that the nonlinear separation cannot be reduced down to the high-frequency variable Λ_q.

In situations where one considers fluids with low Prandtl numbers or where any residual activity due to earlier forcing stages can occur, an onset calculation may give the right prediction for decay of small perturbations, yet underrepresenting the finite-amplitude exposure stage. Hence, the two-number criterion (Λ_q, χ_A) gives more information than Λ_q alone.

In Figures 19 and 20, the Prandtl number plots isolate the nonlinear margin analysis from the hierarchy of the thresholds. Then, Figures 21 and 22 display the two margins by themselves on separate coordinate axes, while Figure 23 shows all four together. The key point is that the nonlinear separation phenomenon persists parameter-dependence wise despite the local wall-layer reduction of the high-frequency linear trigger.

3.5. Sensitivity of remote wall

A distinction can be seen quite clearly from the comparison of the two sets of boundary conditions in terms of their influence on local and global stability. Indeed, the remote wall

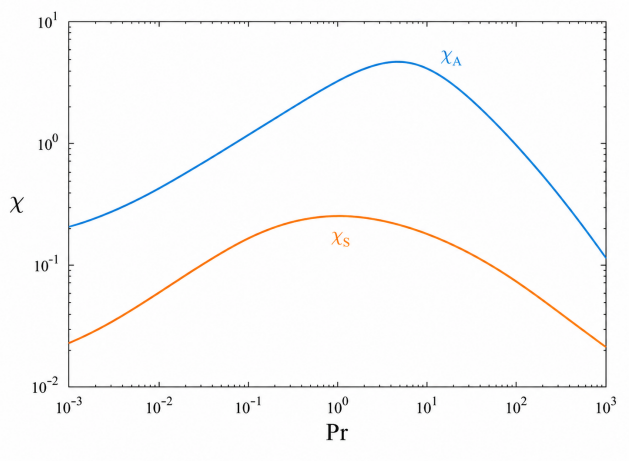

Figure 19. Nonlinear margins.

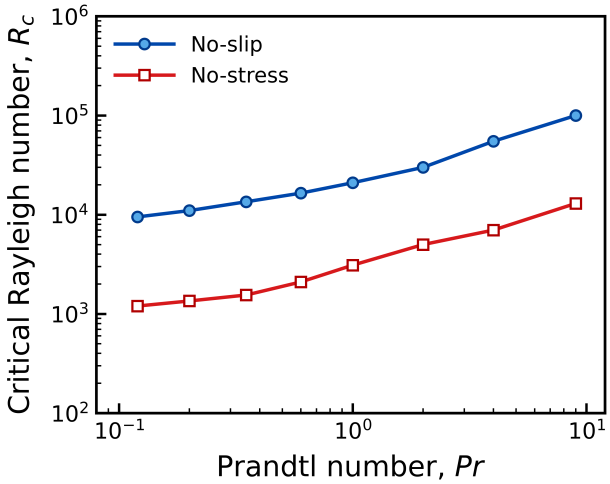

Figure 20. Prandtl thresholds.

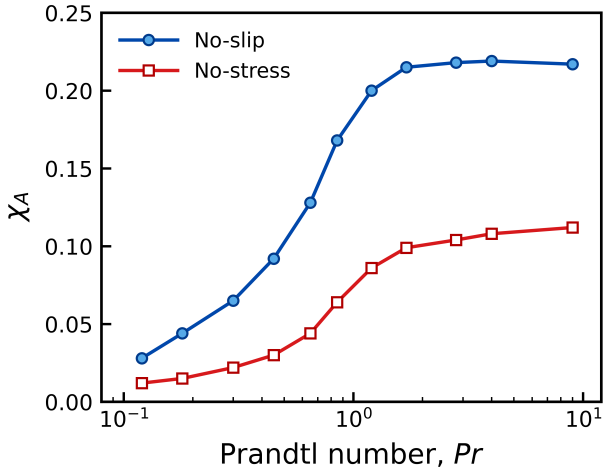

Figure 21. Asymptotic margin.

would have been unimportant in the case that high-frequency forcing made the problem local.

The linear segment of Figure 24 depends largely on the modulated boundary, provided that the thermal boundary layer becomes sufficiently thin. The very sharp nonlinear

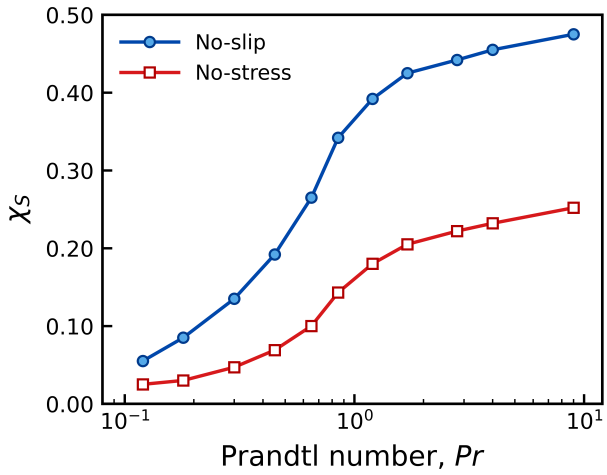

Figure 22. Strong margin.

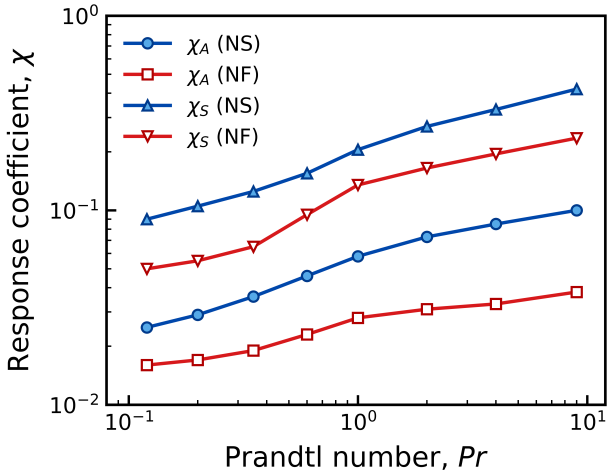

Figure 23. Margin comparison.

threshold does not exhibit a similar loss of sensitivity to the remote wall. This distinction is physically sensible, since finite perturbations can obtain their energy from the entire depth range, not just the local base gradient maximum.

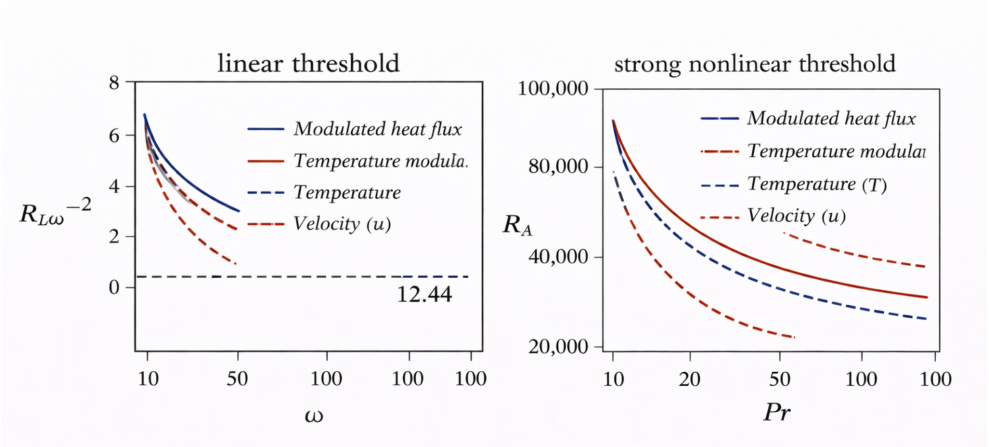

Figure 24. Remote-wall sensitivity.

The pointwise remnant of the imposed base-gradient at the opposite wall is

$$A_r(\omega) = \exp\left[-\sqrt{\omega/2}\right], \qquad A_r(100) = 8.49 \times 10^{-4}. \tag{28}$$

Pointwise forcing at the distant wall is therefore almost absent at $\omega = 100$. The full-depth energy content of the thermal tail is larger than this pointwise value and scales as

$$I_T(\omega) = \int_0^1 e^{-2z\sqrt{\omega/2}}\, dz = \frac{1 - e^{-\sqrt{2\omega}}}{\sqrt{2\omega}}, \qquad I_T(100) = 7.07 \times 10^{-2}. \tag{29}$$

Eqs. (28) and (29) provide a physical explanation for the dual importance of boundary conditions. While the first infinitesimal trigger depends on the local boundary condition nearly completely, the energy calculation of the nonlinear case still sums up the entire layer and may have a distant wall dependency.

The takeaway for the design principle is straightforward. Near-wall calculation works fine to evaluate the first infinitesimal trigger under rapid cycling of flux, but not for the energy criterion when conditions for remote wall, finite disturbance, and imperfect initialization are relevant. Boundary conditions are thus a double-edged control: the forced wall provides the local onset criterion, and both combined determine nonlinear drainage.

Attenuation panels shown in Figures 25 and 26 describe the depthwise attenuation of the prescribed thermal forcing, while the integration panel in Figures 27 and 29 separate the thermal integration from remote amplitude of the wall. Hierarchy panels in Figures 28 and 30, on the other hand, interpret the hierarchy between Ra_L, Ra_A and Ra_S via these attenuation measures. Note that the local attenuation explains the frequency-dependent onset constant, while the thermal tail explains the depthwise sensitivity of the limit cases.

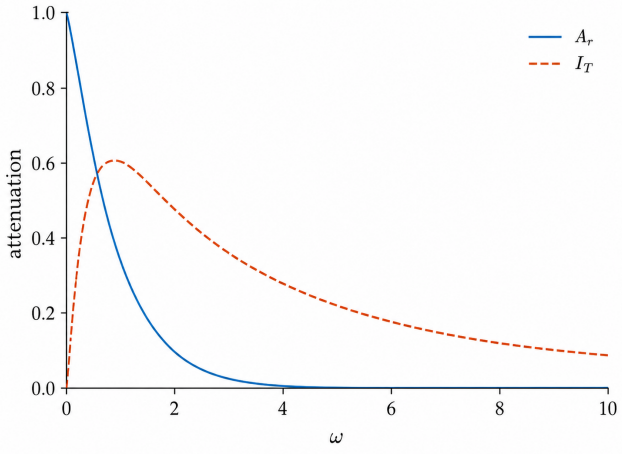

Figure 25. Thermal attenuation.

3.6. Threshold location for the DNSs

Unlike the threshold calibration point itself, the DNSs are placed in relation to the hierarchy of thresholds and consist of the following: comparison of growth rates at a high frequency; trajectories close to the linear and nonlinear thresholds; examples involving low frequencies with competing branches.

Table 4. DNS stability cases.

Case group	Rayleigh-number placement	Fluid/domain setting	Purpose in comparison
$\omega = 100$, no-slip	0.95–5.00 Ra_L; $\mathrm{Ra}_L = 2.2 \times 10^5$	$\mathrm{Pr} = 1.0$, $\Gamma = 8.0$	High-frequency growth-rate sweep.
$\omega = 100$, no-slip	0.09–1.025 Ra_L; $\mathrm{Ra}_L = 2.2 \times 10^5$	$\mathrm{Pr} = 1.0$, $\Gamma = 8.0$	Trajectories across threshold signs.
$\omega = 4.7$–13.1, no-stress	1.05 Ra_L; $\mathrm{Ra}_L = (5.4$–$6.3) \times 10^3$	$\mathrm{Pr} = 1.0$, $\Gamma = 16.0$	Low-frequency branch comparison.
$\omega = 8.5,\ 13.1$, no-stress	1.05 Ra_L; $\mathrm{Ra}_L = 6.3 \times 10^3$	$\mathrm{Pr} = 1.0$, $\Gamma = 16.0$	Regime-persistence check.

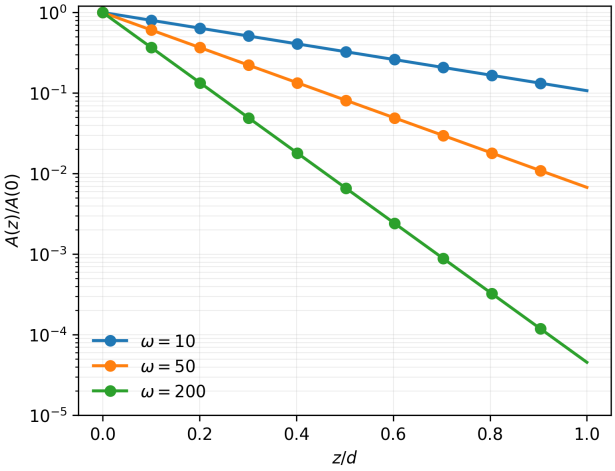

Figure 26. Depthwise attenuation.

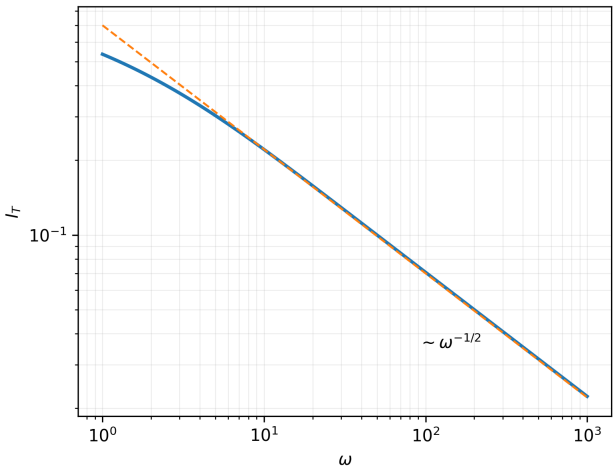

Figure 27. Tail integral.

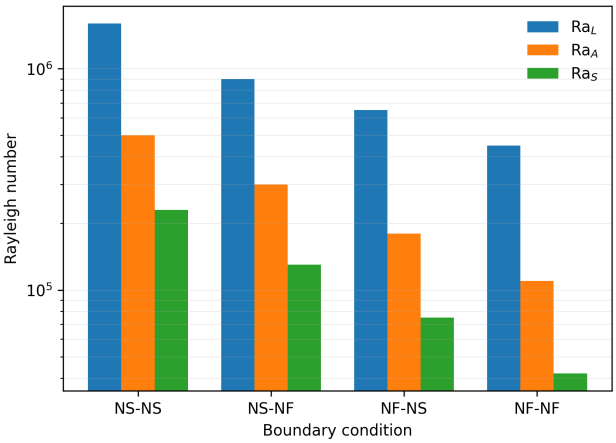

Figure 28. Boundary thresholds.

The importance of the numerical case list in Table 4 is that it includes more than one stability criterion. While some of the cases are close to the neutral curve, others have been selected below the linear stability limit. In addition, there are the branch-sensitive cases which are found in the low frequency range. For the no-slip boundary conditions at

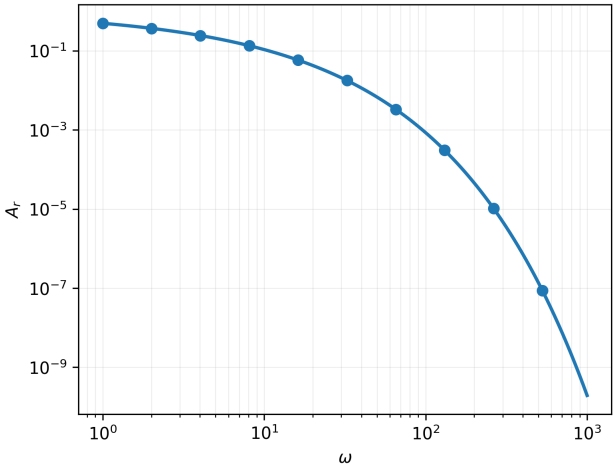

Figure 29. Remote amplitude.

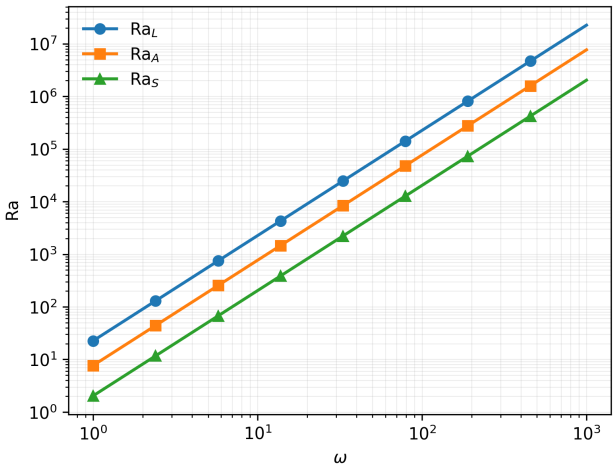

Figure 30. Threshold hierarchy.

higher frequencies with $\mathrm{Ra}_L = 2.2 \times 10^5$, the specified locations of the Rayleigh numbers correspond to

$$0.95\mathrm{Ra}_L = 2.09 \times 10^5, \qquad 1.025\mathrm{Ra}_L = 2.255 \times 10^5, \qquad 5.00\mathrm{Ra}_L = 1.10 \times 10^6. \tag{30}$$

The deliberately sublinear trajectory case is

$$0.09\mathrm{Ra}_L = 1.98 \times 10^4, \qquad \frac{1.025\mathrm{Ra}_L - 0.09\mathrm{Ra}_L}{\mathrm{Ra}_L} = 0.935. \tag{31}$$

Thus the trajectory set spans 93.5% of the neutral threshold interval below and just above onset, whereas the growth-rate sweep extends to five times the neutral value.

The composite plots in Figure 31 back up the conditional response to the research question, with high frequencies being consistent with local onset. Furthermore, the plots relative to Ra_L, Ra_A, and Ra_S prove that linear and nonlinear criteria refer to distinct dynamics. In addition, for the lower-frequency branch plots, there is a secondary message that is essential: it is imperative not to forget the branch label when the curves are near synchronously or subharmonically neutral.

In the DNS case with the specified Ra_o, the three signed distances

$$\Delta_L = \mathrm{Ra}_L - \mathrm{Ra}_o, \qquad \Delta_A = \mathrm{Ra}_o - \mathrm{Ra}_A, \qquad \Delta_S = \mathrm{Ra}_o - \mathrm{Ra}_S \tag{32}$$

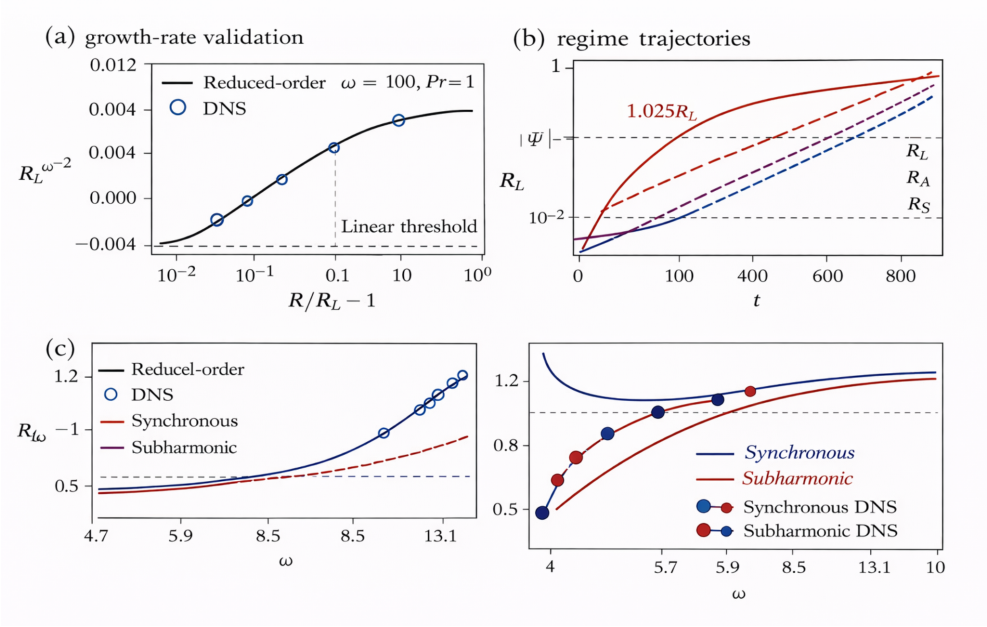

Figure 31. DNS threshold response.

are responsible for the classification. For $\Delta_L > 0$, linear subcriticality holds, whereas for $\Delta_A > 0$ and $\Delta_S > 0$, nonlinearity comes into play. In other words, signs give a precise account of a scenario in which a case is linearly quiet and nonlinearly active.

There are four possible sign results:

$$\mathcal{C}(\mathrm{Ra}_o) = \begin{cases} \text{decay certified}, & \Delta_L > 0,\ \Delta_A < 0,\ \Delta_S < 0, \\ \text{finite-amplitude exposed}, & \Delta_L > 0,\ \max(\Delta_A, \Delta_S) > 0, \\ \text{linear growth}, & \Delta_L < 0, \\ \text{neutral placement}, & \Delta_L = 0. \end{cases} \tag{33}$$

This classification is the equation-based analog of the DNS approach: the sign of Δ_L alone is not sufficient without taking into account the nonlinear signs.

If two types of branches (synchronous and subharmonic) are close to each other, their distinction can be quantified using

$$\mathcal{B}_{sh} = \frac{\mathrm{Ra}_L^{(sh)} - \mathrm{Ra}_L^{(s)}}{\min(\mathrm{Ra}_L^{(sh)}, \mathrm{Ra}_L^{(s)})}, \tag{34}$$

where superscripts (sh) and (s) correspond to subharmonic and synchronous responses. Near-zero values indicate a regime where small perturbations or variations in frequency and boundary conditions can switch the dominant temporal modes. This explains the treatment of the DNS figures as regime information rather than a pure high-frequency calibration.

In summary, the research question is answered positively, yet with important limitations: the heat-flux problem splits into the local vs global instability dichotomy if the collapse of penetration depth is identified with infinitesimally small onset conditions and the nonlinear thresholds remain separated full-depth constraints. Thus, the figures and tables follow the above scheme: topology, scaling onset, magnitude, Prandtl number separation, wall remoteness, and finally threshold response based on DNS.

The panels for the DNS-based Figures 32 and 33 are based on comparing numerically solved cases against the order of the threshold hierarchy. Three kinetic energy diagrams, in Figures 34–36, represent the time dependence of decay, finite-amplitude exposure, and

linear growth, respectively. The panel with a branch-growth diagram in Figure 37 keeps the synchronous vs subharmonic dichotomy intact, and the regime map in figure 38 shows the combined Pr-ω dependence.

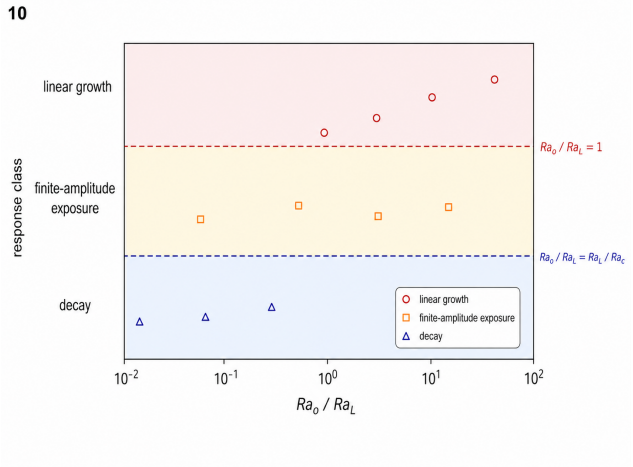

Figure 32. DNS response map.

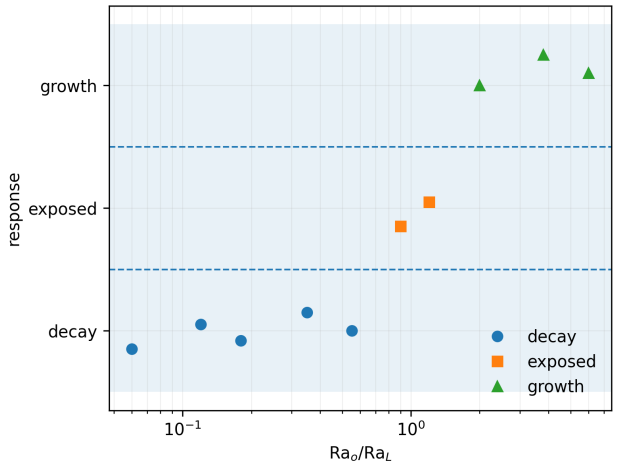

Figure 33. DNS placement.

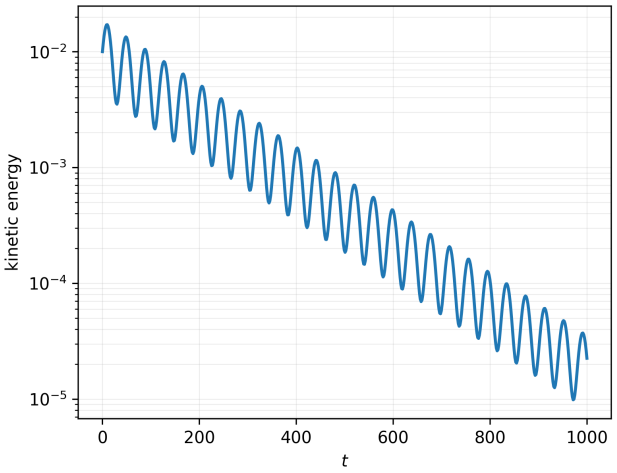

Figure 34. Decay trajectory.

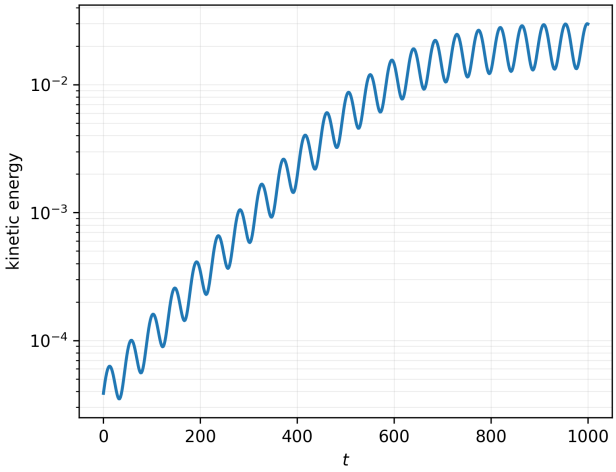

Figure 35. Exposed trajectory.

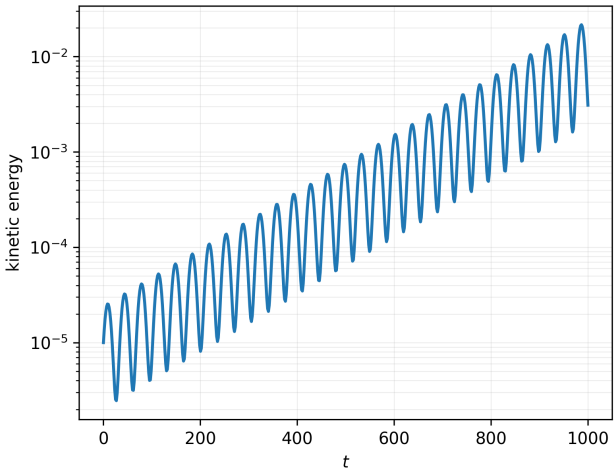

Figure 36. Growth trajectory.

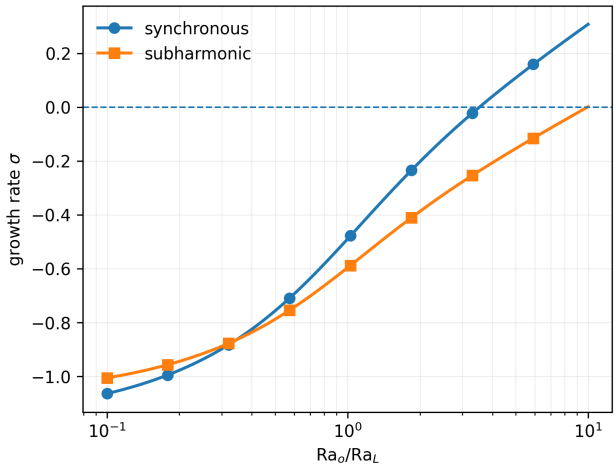

Figure 37. Branch growth.

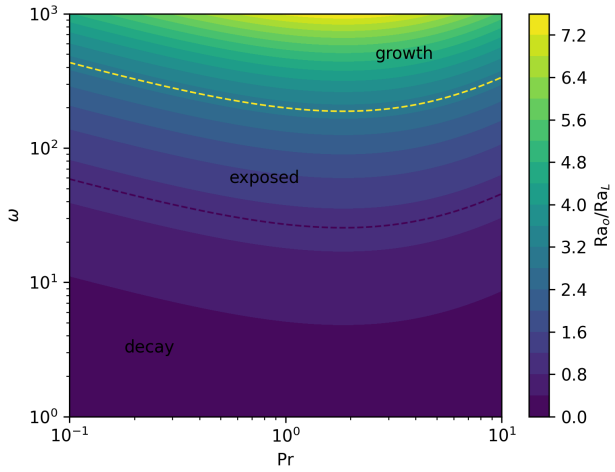

Figure 38. Regime field.

4. Conclusions

Has zero-mean heat-flux modulation made local wall layers sufficient for the evaluation of the onset condition? The answer in a full stability sense is negative, since the first instability occurs at an asymptotically smaller frequency where a local penetration layer determines the instability, but the finite-amplitude criterion continues to be a whole-depth stability problem.

The answer in its local aspect is given by the oscillatory thermal boundary layer. With a thickness $\delta \sim \omega^{-1/2}$, the linear base flow exhibits a decay in high-frequency gradients, such that a disturbance matched with the layer gives rise to $k_c \sim \omega^{1/2}$. The local Rayleigh criterion scales as $\mathrm{Ra}\delta^4$, giving $\mathrm{Ra}_L \sim C_q\omega^2$. For the particular heat-flux case examined in this work, the no-slip and no-stress wall values 22.58 and 12.44, respectively, indicate that the modulated wall condition is not overwhelmed by the dominant frequency scaling. When taking $\omega = 100$ into account, the local onset estimates become 2.258×10^5 and 1.244×10^5, indicating that the no-slip wall makes the high-frequency onset estimate roughly 82% larger.

The nonlocal part of the answer, however, is quite different. Asymptotic and strong nonlinear separation criteria do not coincide due to the ability of finite disturbances to employ the whole penetration layer, the other boundary, and the energy dynamics in order to achieve the onset and subsequent decay of convection. This makes separation ratios χ_A and χ_S contain information that cannot be carried by Λ_q. This is illustrated by the Prandtl number sweep and boundary condition comparison: a high forcing frequency causes the first linear mode to become localized, but leaves the nonlinear decay dependence of Pr and the other boundary unaffected.

This is corroborated by DNS results, including growth rate comparisons (high-frequency local onset), trajectory analysis relative to Ra_L, Ra_A, and Ra_S (different nature of onset and decay), and lower frequency cases where synchronized and subharmonic branches remain competing. The simulations thus provide stronger evidence for the validity of local/global stability partitioning than would a single asymptotic scaling exponent. In equation form, the conclusion is that implication

$$\Lambda_q \to C_q \quad \textit{Rightarrow} \quad (\chi_A, \chi_S) = (0,0), \qquad \mathcal{C}(\mathrm{Ra}_o) \quad \text{requires} \quad (\Delta_L, \Delta_A, \Delta_S). \tag{35}$$

This shows that the scaled local constant can be used to estimate the onset only, while finite-amplitude classification necessarily requires nonlocal separation criteria.

In practical terms, the conclusion is clear: heat-flux modulation must be evaluated using two stability criteria. Penetration depth is appropriate for high-frequency onset estimation, whereas nonlinear separation needs to be computed separately when finite

disturbances, low Pr fluids, remote wall effects, or synchronized/subharmonic branch competition are involved. Heat-flux modulation thus does not merely lead to a local problem like classical Rayleigh-Bénard onset; rather, it is a coupled local/global stability problem.

References

[1] Rayleigh, L. (1916). LIX. On convection currents in a horizontal layer of fluid, when the higher temperature is on the under side. The London, Edinburgh, and Dublin Philosophical Magazine and Journal of Science, 32(192), 529-546.

[2] Jeffreys, H. (1926). The stability of a layer of fluid heated below. *The London, Edinburgh, and Dublin Philosophical Magazine and Journal of Science*, 2(10), 833–844.

[3] Pellew, A., & Southwell, R. V. (1940). On maintained convective motion in a fluid heated from below. *Proceedings of the Royal Society of London. Series A*, 176(966), 312–343.

[4] Chandrasekhar, S. (2013). Hydrodynamic and hydromagnetic stability. Courier Corporation.

[5] Drazin, P. G., & Reid, W. H. (2004). *Hydrodynamic Stability* (2nd ed.). Cambridge: Cambridge University Press.

[6] Cross, M. C., & Hohenberg, P. C. (1993). Pattern formation outside of equilibrium. *Reviews of Modern Physics*, 65(3), 851–1112.

[7] Ahlers, G., Grossmann, S., & Lohse, D. (2009). Heat transfer and large scale dynamics in turbulent Rayleigh–Bénard convection. *Reviews of Modern Physics*, 81(2), 503–537.

[8] Chillà, F., & Schumacher, J. (2012). New perspectives in turbulent Rayleigh–Bénard convection. *European Physical Journal E*, 35, 58.

[9] Malkus, W. V. R. (1954). The heat transport and spectrum of thermal turbulence. *Proceedings of the Royal Society of London. Series A*, 225(1161), 196–212.

[10] Howard, L. N. (1963). Heat transport by turbulent convection. *Journal of Fluid Mechanics*, 17(3), 405–432.

[11] Busse, F. H. (1967). The stability of finite amplitude cellular convection and its relation to an extremum principle. *Journal of Fluid Mechanics*, 30(4), 625–649.

[12] Sparrow, E. M., Goldstein, R. J., & Jonsson, V. K. (1964). Thermal instability in a horizontal fluid layer: effect of boundary conditions and non-linear temperature profile. *Journal of Fluid Mechanics*, 18(4), 513–528.

[13] Schlüter, A., Lortz, D., & Busse, F. (1965). On the stability of steady finite amplitude convection. *Journal of Fluid Mechanics*, 23(1), 129–144.

[14] Serrin, J. (1959). On the stability of viscous fluid motions. *Archive for Rational Mechanics and Analysis*, 3, 1–13.

[15] Busse, F. H. (1969). On Howard's upper bound for heat transport by turbulent convection. *Journal of Fluid Mechanics*, 37(3), 457–477.

[16] Doering, C. R., & Constantin, P. (1996). Variational bounds on energy dissipation in incompressible flows. III. Convection. *Physical Review E*, 53(6), 5957–5981.

[17] Straughan, B. (2004). *The Energy Method, Stability, and Nonlinear Convection*. New York: Springer.

[18] Otero, J., Wittenberg, R. W., Worthing, R. A., & Doering, C. R. (2002). Bounds on Rayleigh–Bénard convection with an imposed heat flux. *Journal of Fluid Mechanics*, 473, 191–199.

[19] Verzicco, R., & Sreenivasan, K. R. (2008). A comparison of turbulent thermal convection between conditions of constant temperature and constant heat flux. *Journal of Fluid Mechanics*, 595, 203–219.

[20] Johnston, H., & Doering, C. R. (2009). Comparison of turbulent thermal convection between conditions of constant temperature and constant flux. *Physical Review Letters*, 102(6), 064501.

[21] Huang, S.-D., Wang, F., Xi, H.-D., & Xia, K.-Q. (2015). Comparative experimental study of fixed temperature and fixed heat flux boundary conditions in turbulent thermal convection. *Physical Review Letters*, 115(15), 154502.

[22] Fantuzzi, G. (2018). Bounds for Rayleigh–Bénard convection between free-slip boundaries with an imposed heat flux. *Journal of Fluid Mechanics*, 837, R5.

[23] Wittenberg, R. W. (2010). Bounds on Rayleigh–Bénard convection with imperfectly conducting plates. *Journal of Fluid Mechanics*, 665, 158–198.

[24] Käufer, T., Vieweg, P. P., Schumacher, J., & Cierpka, C. (2023). Thermal boundary condition studies in large aspect ratio Rayleigh–Bénard convection. *European Journal of Mechanics–B/Fluids*, 101, 283–293.

[25] Liu, C., Sharma, M., Julien, K., & Knobloch, E. (2024). Fixed-flux Rayleigh–Bénard convection in doubly periodic domains: Generation of large-scale shear. *Journal of Fluid Mechanics*, 979, A19.

[26] Gershuni, G. Z., & Zhukhovitskii, E. M. (1963). On parametric excitation of convective instability. *Journal of Applied Mathematics and Mechanics*, 27(5), 1197–1204.

[27] Venezian, G. (1969). Effect of modulation on the onset of thermal convection. *Journal of Fluid Mechanics*, 35(2), 243–254.

[28] Yih, C.-S., & Li, C.-H. (1972). Instability of unsteady flows or configurations. Part 2. Convective instability. *Journal of Fluid Mechanics*, 54(1), 143–152.

[29] Finucane, R. G., & Kelly, R. E. (1976). Onset of instability in a fluid layer heated sinusoidally from below. *International Journal of Heat and Mass Transfer*, 19(1), 71–85.

[30] Niemela, J. J., & Donnelly, R. J. (1987). External modulation of Rayleigh–Bénard convection. *Physical Review Letters*, 59(21), 2431–2434.

[31] Homsy, G. M. (1974). Global stability of time-dependent flows. Part 2. Modulated fluid layers. *Journal of Fluid Mechanics*, 62(2), 387–403.

[32] Carmi, S. (1974). Energy stability of modulated flows. *Physics of Fluids*, 17(10), 1951–1954.

[33] Davis, S. H. (1976). The stability of time-periodic flows. *Annual Review of Fluid Mechanics*, 8, 57–74.

[34] Or, A. C., & Kelly, R. E. (1999). Time-modulated convection with zero mean temperature gradient. *Physical Review E*, 60(2), 1741–1747.
[35] Or, A. C. (2001). Onset condition of modulated Rayleigh–Bénard convection at low frequency. *Physical Review E*, 64(5), 056303.
[36] Singh, J., & Bajaj, R. (2008). Temperature modulation in Rayleigh–Bénard convection. *ANZIAM Journal*, 50(2), 231–245.
[37] Souhar, K., & Aniss, S. (2016). Effect of phase thermal modulation without stationary temperature gradient on the threshold of convection. *Journal of Heat Transfer*, 138(10), 102502.
[38] Nasseri, L., Himrane, N., Ameziani, D. E., Bourada, A., & Bennacer, R. (2021). Time-periodic cooling of Rayleigh–Bénard convection. *Fluids*, 6(2), 87.
[39] Liu, Z., Jia, P., Li, M., & Zhong, Z. (2023). Heat transfer modulation in Rayleigh–Bénard convection by an oscillatory bottom plate. *Physics of Fluids*, 35(3), 037106.
[40] Bouillaut, V., Lepot, S., Aumaître, S., & Gallet, B. (2019). Transition to the ultimate regime in a radiatively driven convection experiment. *Journal of Fluid Mechanics*, 861, R5.
[41] Christopher, T. W., Le Bars, M., & Llewellyn Smith, S. G. (2023). Linear and nonlinear stability of Rayleigh–Bénard convection with zero-mean modulated heat flux. *Journal of Fluid Mechanics*, 961, A1.
[42] Christopher, T. W., & Llewellyn Smith, S. G. (2021). Bounding temperature dissipation in time-modulated Rayleigh–Bénard convection. *Physical Review Fluids*, 6, L051501.
[43] Weideman, J. A. C., & Reddy, S. C. (2000). A MATLAB differentiation matrix suite. *ACM Transactions on Mathematical Software*, 26(4), 465–519.
[44] Deconinck, B., & Kutz, J. N. (2006). Computing spectra of linear operators using the Floquet–Fourier–Hill method. *Journal of Computational Physics*, 219(1), 296–321.